NASA/TM–20205009645

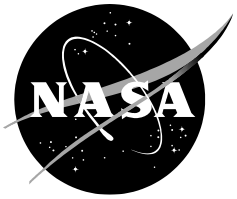

Novel Fiber Optic Sensing Arrays with Enhanced Sensitivity in Cryogenic Temperatures

Hon Man Chan
Armstrong Flight Research Center, Edwards, California

August 2021

NASA STI Program Report Series

The NASA STI Program collects, organizes, provides for archiving, and disseminates NASA's STI. The NASA STI program provides access to the NTRS Registered and its public interface, the NASA Technical Reports Server, thus providing one of the largest collections of aeronautical and space science STI in the world. Results are published in both non-NASA channels and by NASA in the NASA STI Report Series, which includes the following report types:

- TECHNICAL PUBLICATION. Reports of completed research or a major significant phase of research that present the results of NASA Programs and include extensive data or theoretical analysis. Includes compilations of significant scientific and technical data and information deemed to be of continuing reference value. NASA counterpart of peer-reviewed formal professional papers but has less stringent limitations on manuscript length and extent of graphic presentations.

- TECHNICAL MEMORANDUM. Scientific and technical findings that are preliminary or of specialized interest, e.g., quick release reports, working papers, and bibliographies that contain minimal annotation. Does not contain extensive analysis.

- CONTRACTOR REPORT. Scientific and technical findings by NASA-sponsored contractors and grantees.

- CONFERENCE PUBLICATION. Collected papers from scientific and technical conferences, symposia, seminars, or other meetings sponsored or co-sponsored by NASA.

- SPECIAL PUBLICATION. Scientific, technical, or historical information from NASA programs, projects, and missions, often concerned with subjects having substantial public interest.

- TECHNICAL TRANSLATION. English-language translations of foreign scientific and technical material pertinent to NASA's mission.

Specialized services also include organizing and publishing research results, distributing specialized research announcements and feeds, providing information desk and personal search support, and enabling data exchange services.

For more information about the NASA STI program, see the following:

- Access the NASA STI program home page at http://www.sti.nasa.gov

- Help desk contact information:

https://www.sti.nasa.gov/sti-contact-form/ and select the "General" help request type.

NASA/TM–20205009645

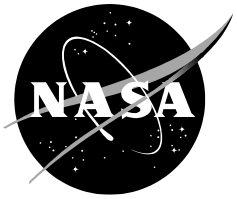

Novel Fiber Optic Sensing Arrays with Enhanced Sensitivity in Cryogenic Temperature

Hon Man Chan
Armstrong Flight Research Center, Edwards, California

National Aeronautics and
Space Administration

Armstrong Flight Research Center
Edwards, California 93523-0273

August 2021

Acknowledgments

I express my gratitude to my colleagues at the National Aeronautics and Space Administration (NASA), who made this work possible. Thank you to Allen Parker, Anthony Piazza, and Dr. W. Lance Richards at the Armstrong Flight Research Center (AFRC) (Edwards, California) for their pioneering work on the distributed fiber-optic sensing interrogator, novel sensing techniques, and strain-based shape-sensing, respectively. I acknowledge Wesley Johnson at the NASA Glenn Research Center (GRC) (Cleveland, Ohio) for his valuable insights on cryogenic temperature measurement, as well as Ali Kashani at the NASA Ames Research Center (ARC) (Moffett Field, California), and James Smith at the NASA Marshall Space Flight Center (MSFC) (Huntsville, Alabama) and their team for much help and support. Thank you to Eric Miller, John Del Frate, and the Fiber Optic Sensing System (FOSS) team at AFRC for many valuable discussions.

.

Abstract

State-of-the-art instrumentation techniques have provided an opportunity to obtain greater insight into the characteristics of cryogenic liquid storage. Optical fiber sensors that utilize fiber Bragg gratings are a viable option for temperature sensing in volatile liquid such as liquid oxygen because there is no risk of electrical sparking and no electromagnetic interference. The National Aeronautics and Space Administration (NASA) Armstrong Flight Research Center (Edwards, California) has developed a novel, simple-to-fabricate fiber array sensor that has been tested and found to be three times more sensitive than typical fiber sensors under cryogenic condition (traditional fiber sensors can suffer from reduced sensitivity below 100 K). Cryogenic temperature monitoring using the NASA fiber optic sensing system is demonstrated in a simulated cryostatic condition, as well as in an elevated pressure environment under liquid nitrogen. Measurement accuracy is compared with traditional silicon diodes. Instrument installation, sensor characteristics, and experimental results are discussed in detail.

Nomenclature

AFRC	Armstrong Flight Research Center
ARC	Ames Research Center
A.U.	arbitrary unit
BBR	broadband reflector
CTE	coefficient of thermal expansion
EMI	electromagnetic interference
FBG	fiber Bragg grating
FFT	Fast Fourier Transform
FOSS	fiber optic sensing system
iFFT	inverse Fast Fourier Transform
ID	inner diameter
k	gage factor
LN_2	liquid nitrogen
LO	local oscillator
nm	nanometer
n_e	effective index of refraction of FBG
NASA	National Aeronautics and Space Administration
OFDR	optical frequency domain reflectometry
pm	picometer
ppm	parts per million
psig	pound-square-inches, gage
PT	cryostat internal pressure
PTFE	polytetrafluoroethylene
SD	silicon diode
STD	standard
T	temperature
TC	thermocouple
WDM	wavelength-division multiplexing
α_{CTE}	coefficient of thermal expansion, *m/K*
α_n	thermo optic coefficient of FBG fiber core, *1/K*
ΔL	change in length of material, *m/m*
ΔT	change in temperature

Δλ	change in wavelength
$\Delta\lambda_B$	change in Bragg wavelength due to environmental change, *m*
ε	strain
ε_m	mechanical strain, *m/m*
ε_T	thermal strain, *m/m*
λ	wavelength
λ_0	initial Bragg wavelength of FBG, *m*
λ_B	center Bragg wavelength of FBG, *m*
Λ	pitch length of FBG, *m*
ρ_e	strain optic coefficient of FBG

Introduction

Cryogenic fluid management plays an important role in the National Aeronautics and Space Administration (NASA) road map toward space exploration. Under the NASA In-Situ Resources Utilization (ISRU), lunar ice residing in the polar region may be extracted, and, through liquefaction, liquid oxygen could be recovered from that ice and stored for future lunar rocket deployment. An accurate, reliable method by which to assess the amount of liquid propellant that is generated thus becomes important for future NASA lunar missions. Cryogenic liquid level measurement also can be beneficial for long-term spacecraft operation, providing the ability to measure the amount of liquid propellant present during and after fuel-burn maneuvers. Traditional cyrogenic temperature sensors that utilize an array of silicon diodes can become cumbersome for installation and deployment because of the myriad of wires that is necessary to power and operate them. Optical fiber sensors that utilize fiber Bragg gratings (FBGs) are not powered by electrical current, and thus are a viable option for temperature sensing in volatile liquid because there is no risk of electrical sparking and no electromagnetic interference (EMI). An array of FBGs can be simultaneously sampled with only a single fiber optic cable, with spatial resolution down to approximately 0.25 in, by utilizing optical frequency domain refractometry (OFDR) interrogation technology. Traditional fiber optic sensors, however, suffer from reduced sensor responsivity under cryogenic condition, which diminishes the temperature accuracy of the fiber sensor. The NASA Armstrong Flight Research Center (AFRC) (Edwards, California) has integrated a cold-compression support sleeve that enhances the temperature sensitivity of the traditional fiber sensor under cryogenic conditions.

This report presents an introduction to FBG sensing, as well as a brief overview of OFDR interrogation technology. The problem of how FBG sensing becomes ineffective under cryogenic conditions is discussed. Fabrication of the cold-compression support sleeve is described, as is the testing of the enhanced fiber sensor under cryogenic condition using a simulated cryostatic chamber. Immersion testing under liquid nitrogen in an elevated pressure environment is described. Experimental results demonstrate that the enhanced fiber sensor is three times more sensitive under cryogenic condition than the traditional fiber sensor; this new technology thus could be a viable candidate for temperature and liquid-level monitoring in a volatile and cryogenic environment.

Fiber Bragg Grating Theory

Optical fiber, which is widely used in telecommunications, is composed of a cylindrical waveguide with a narrow core and a much larger cladding layer with a slightly higher refractive index; the refractive index is based on the composition of doped Germanium (Ge) within the fused-silica fiber core. By the principle of total internal refraction, light can propagate many miles through the fiber core with little optical attenuation; and, by periodically changing the refractive

index of a section of the FBG, a notch filter that reflects a specific wavelength can be created. Fabrication of FBGs involves exposing sections of optical fiber to an ultraviolet laser; the laser passes through a special phase mask of a specific pitch in order to create a pattern. As portions of the fiber core react to the laser light, which excites the doped Ge to rearrange within the fiber core, a change of refractive index results. The phase-mask-induced pattern exposure results in a periodic change of index of refraction through a section of fiber, which results in the creation of an FBG.

In telecommunications, FBGs work as reflective filter wherein the pitch length of the grating (Λ) determines the particular wavelength at which the signal will be reflected, as shown in equation (1):

$$\lambda_B = 2n_e\Lambda \tag{1}$$

where λ_B is the center Bragg wavelength of the FBG, and n_e is the effective index of refraction of the FBG. From equation (1), the center wavelength of the grating is determined by the pitch length of the grating, which is affected by environmental perturbation such as structural bending or temperature-related contraction or expansion. By monitoring the change of the center wavelength of the grating over its initial wavelength at ambient condition, an FBG can be used as either a strain sensor or a temperature sensor, as shown in equation (2).

$$\frac{\Delta\lambda_B}{\lambda_0} = (1-\rho_e)\varepsilon + \alpha_n\Delta T \tag{2}$$

$\Delta\lambda_B = (\lambda_B - \lambda_0)$ → the change in Bragg wavelength due to environmental change
λ_0= the initial Bragg wavelength of the FBG
ρ_e= the strain optic coefficient, 0.833, of the FBG
α_n = the thermo-optic coefficient of the fiber core at room temperature (ref. 1): 8.6 x 10^{-6} /K

From equation (2), it can be seen that the Bragg wavelength change in the FBG is affected by strain (ε) change as well as by the thermal gradient (ΔT). Additional, strain change can be caused by mechanical and thermal components, as shown in equations (3):

$$\begin{aligned} \varepsilon &= \varepsilon_m + \varepsilon_T \\ \varepsilon &= \varepsilon_m + \alpha_{CTE}\Delta T \end{aligned} \tag{3}$$

where ε_m is the mechanical strain, based on the amount of length being stretched or compressed, or $\varepsilon_m = \frac{\Delta L}{L}$. The thermal strain is represented by ε_T, and α_{CTE} (CTE, coefficient of thermal expansion) describes how the material contracts or expands when being cooled or being heated. In the context of utilizing an FBG as a temperature sensor, it is advantageous to eliminate any outside mechanical strain component affecting the FBG in order to achieve an accurate temperature relationship. Recalling equation (2) and assuming $\varepsilon_m = 0$; equation (4) can be constructed.

$$\begin{aligned} \frac{\Delta\lambda_B}{\lambda_0} &= (1-\rho_e)(\varepsilon_m + \alpha_{CTE}\Delta T) + \alpha_n\Delta T \\ \frac{\Delta\lambda_B}{\lambda_0} &= (1-\rho_e)\alpha_{CTE}\Delta T + \alpha_n\Delta T \end{aligned} \tag{4}$$

Next, by combining the temperature change term (ΔT), and assuming that the gage factor $= 1 - \rho_e$; equation (5) can be constructed.

$$\frac{\Delta\lambda_B}{\lambda_0} = (k\alpha_{CTE} + \alpha_n)\Delta T \quad (5)$$

Equation (5) shows that for an FBG to be used as a temperature sensor, both the coefficient of thermal expansion of the fiber (α_{CTE}) and the thermo-optic coefficient of the core (α_n) play a role. Under room temperature (297 K, or 75 °F) with an FBG of initial center wavelength of 1550 nm, pre-degree Kelvin of temperature change results in 7.8 pm of wavelength shift. At this temperature regime, the thermo-optic coefficient (8.6 x 10^{-6} /K) is one magnitude larger than the thermal-expansion coefficient (5.5 x 10^{-7} /K). In subsequent discussion, the CTE plays a much more robust role in the cryogenic regime due to the diminishing effect of the thermo-optic coefficient under cryogenic conditions.

Optical Frequency-Domain Reflectometry

Fiber-optic sensing based on OFDR has been discussed in detail in previous work (ref. 2); a brief summary is included here. Fiber Bragg grating-based sensing typically utilizes the wavelength-division multiplexing (WDM) interrogation technique, shown at the top of figure 1. First, each FBG reflects light unique to its center wavelength from the broadband light source; the reflected center wavelength is actively monitored by a wavelength spectrometer. Wavelength change of a specific FBG over its initial wavelength indicates environmental perturbation (strain or temperature change). One of the problems of FBG sensing using WDM is the limited number of sensors available to sample at the same time. Each FBG needs to possess a unique center wavelength to distinguish from one another, so the total number of sensors that can be interrogated simultaneously is limited due to the limited bandwidth available from the WDM spectrometer.

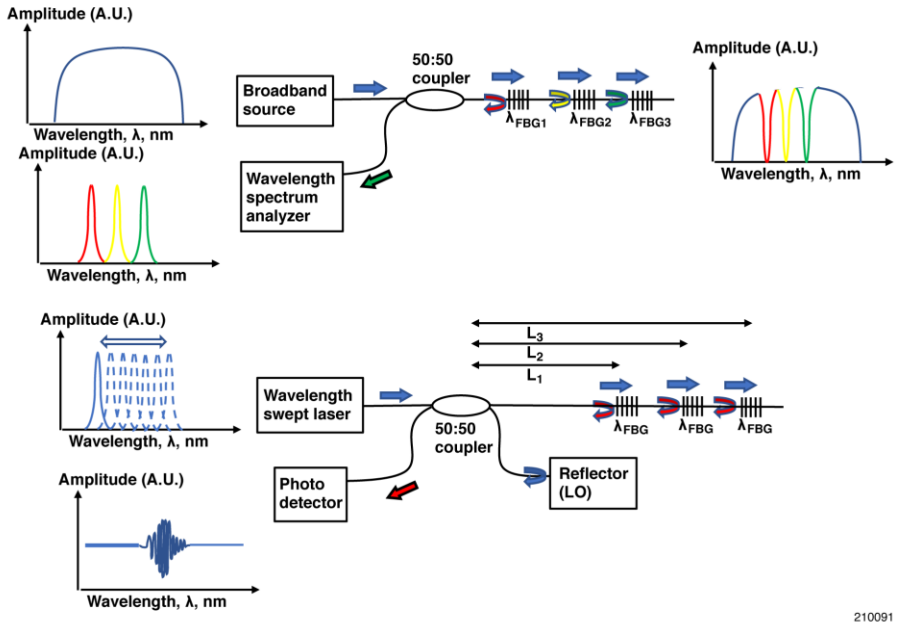

Figure 1. Graphical representation of (top) WDM and (bottom) OFDR FBG sensing scheme. Top: The WDM-based sensing is directly measuring the reflective wavelengths of all the FBGs, each having a unique center wavelength, available in the fiber. A challenge of WDM-based sensing sensors is the potential for grating-to-grating aliasing, wherein measurement uncertainty can occur when the center wavelength of one sensor overlaps with an adjacent sensor. Bottom: The OFDR is based on interference measurement. Despite each FBG under OFDR having the same center wavelength, the difference in location causes a unique beat-frequency that can be identified using Fourier domain transformation.

In comparison, OFDR-based sensing utilizes multiple FBGs with the same center wavelength, shown at the bottom of figure 1. In this scheme, the length difference of each sensor relative to the local oscillator (LO) arm determines the unique identifier, or the beat frequency, of each sensor. In order to distinguish each sensor with its beat frequency, a Fast Fourier Transform (FFT) is conducted on the reflecting signal, encompassing the beat frequency of all reflecting sensors with respect to the LO arm. Once all the unique sensors are identified using Fourier domain, a sensor of interest can be isolated for observation, and an inverse Fast Fourier Transform (iFFT) conducted in order to determine the center wavelength of the sensor. In summary, the WDM is a direct wavelength measurement; the OFDR is an interferometric measurement, where signal processing such as FFT is needed to decode the wavelength of any FBG sensor.

Conducting multiple FTT/iFFT computations in real time can become a major bottleneck in terms of computational speed, so AFRC has developed various computation algorithms, such as short-time Fourier Transfer (ref. 3) as well as wavelet calculation (ref. 4), that simplify the computation process and increase the real-time data acquisition rate. Another advantage of using such algorithms is that FBG sensors now can be discretized as sensing unit-length, where physical location of multiple FBG sensors can be combined to a pre-determined unit-length. In the case of the wavelet algorithm, sensor unit-length can be either shortened or lengthened to compensate for sensor activity: areas of low environmental strain or temperature change can be combined into one sensor, and areas of high environmental change sensor unit-length can be finely discretized, down to the unit length of each physical FBG sensor.

Fiber Optic Sensing System Overview

The NASA fiber optic sensing system (FOSS) describes the complete suite of interrogator-system-in-a-box, shown in figure 2. The FOSS includes the integrated hardware, which contains a continuously-tuned wavelength-swept laser, a custom optical network that can simultaneously sample multiple channels of fiber sensor arrays in real time, and also generates a real-time reference clock (ref. 5). A custom field-programmable gate array (FPGA) chipset runs a custom algorithm to facilitate the FFT/iFFT calculation process. A general-purpose central processing unit (CPU) acts as a server for data storage and data transport; the CPU conducts background tasks such as network transfer of real-time data over Ethernet to multiple clients.

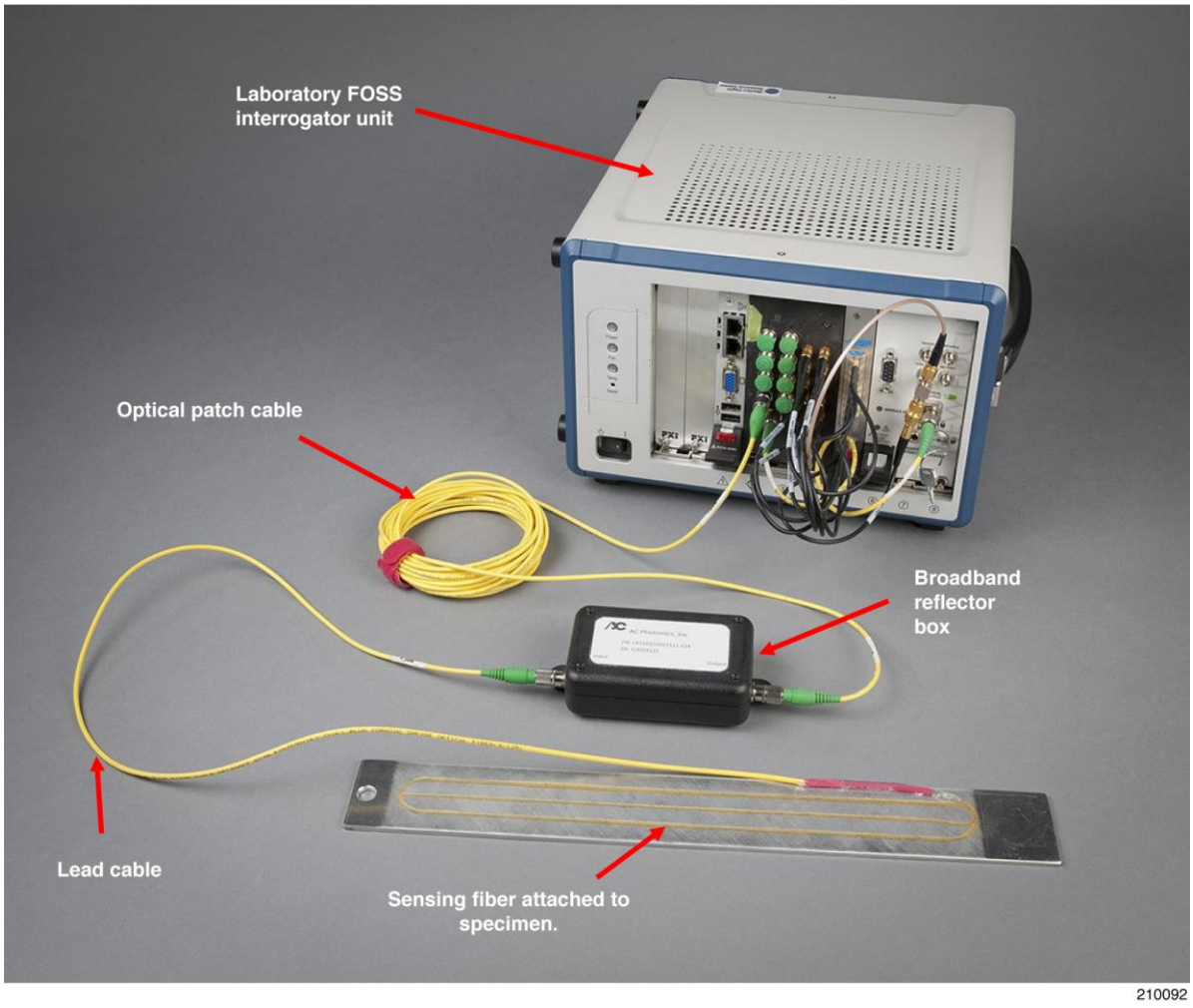

Figure 2. The fiber optic sensing system (FOSS) is comprised of the system-in-a-box hardware interrogator unit, as well as an optical fiber sensing array consisting of multiple low-reflectivity fiber Bragg gratings having the same center wavelength.

Fiber grating array sensors, composed of many FBGs with low reflectivity, is utilized for OFDR sensing. Typical FBG sensors utilized in the WDM scheme have high reflectivity value (> 50%), so that each the center wavelength of each sensor can be identified; however, in OFDR application, each FBG sensor has the same center wavelength as well as a much lower reflectivity (0.01 to 0.001 percent) than typical FBG sensors. As a result, hundreds of identical

sensors can be in the same fiber without incurring significant light loss. In FOSS application, each sensing array can be composed of up to 40 ft of low-reflectivity gratings, connected to an optical interferometer box or a broadband reflector (BBR). The BBR contains the LO arm that marks the beginning distance calculation for each of the sensors. A fiber patch cable, up to 100 ft long, is connected from the FOSS interrogator box to the BBR box, so that the interrogator can be located a long distance away from the sensing - beneficial in combustible or EMI-susceptible environments.

Prior-art Fiber Bragg Grating Response in a Cryogenic Environment

Equation (2) shows that FBGs respond to temperature changes by both the thermo-optic coefficient (α_n) as well as the CTE. The thermo-optic coefficient is defined as changes in the refractive index with respect to temperature change; the CTE is defined as temperature-induced strain caused by either thermal contraction or expansion of the overall fiber, to include the material coating the fiber. At room temperature or at elevated temperature (297 K or above), the thermal response of an FBG is dominated by the thermo-optic coefficient, resulting in an increase in the center wavelength proportional to the temperature increase (ref. 6). If an FBG is deployed in a cryogenic environment, however, the center wavelength rate of change will exponentially decrease from a certain temperature (refs. 7, 8). The tapering-off effect is caused by the lower value of the thermo-optic coefficient at cryogenic temperature. At these low temperatures, the induced strain caused by CTE contraction becomes the dominating force behind the wavelength change. Fiber Bragg grating sensors with polyimide coating, which are suitable for high temperature measurement up to 573 K, have low CTE (20 ppm/K) at room temperature. Fiber Bragg grating sensors with acrylate coating have a relative higher CTE (60 ppm/K); however, they have poor strain transfer value such that the higher CTE value does not translate well in terms of induced strain that may be caused by slippage between coating and cladding (ref. 9).

In order to improve the temperature response of FBGs in a cryogenic environment, it is known that either increasing the CTE value of the coating material or increasing the coating thickness (ref. 10) can achieve desirable results. Temperature response improvement can be achieved by increasing the coating of the fiber (ref. 10), coating the fiber with a metal coating of a higher CTE (ref. 11), or by inducing pre-load strain on the fiber (ref. 12). In this report, a novel method of incorporating a polytetrafluoroethylene (PTFE) layer wrapped on to the outside of the commercial fiber grating array has shown that in cryogenic condition, consistent thermal responsivity down to liquid nitrogen temperature (78 K) can be achieved due to the increased overall thickness as well as the higher CTE of the PTFE wrap. Comparison with calibrated silicon diode under cryostat conditions has shown that fiber sensor array can interrogate temperature down to 15 K. Compared with polyimide-coated fiber sensor, the novel sensor is three times more responsive under liquid nitrogen.

Sensor Fabrication

The prototype of the PTFE-based heat-activated shrink sleeve was applied to the polyimide-coated fiber sensor array. The PTFE shrink sleeve has a pre-shrunk inner diameter (ID) of 500 µm; the relatively large size makes it suitable to route a long length of fiber sensor array (outer diameter 145 µm) with little resistance. Once the fiber is inserted completely into the shrink-sleeve, the entire structure is subjected to a slow temperature ramp (approximately 5 °C/min) from ambient temperature to 340 °C. The PTFE shrink-sleeve begins to activate at 300 °C, when the ID shrinks to 150 µm, to ensure that the sleeve is completely wrapped around the cross-section of the fiber with its coating layers. Afterward, a slow cool-down (approximately 10 °C/min ramp rate until 150 °C) ensures uniform wall thickness throughout the length of the

fiber sensor. The relaxed wall thickness of the PTFE sleeve is approximately 125 µm, which is ten times thicker than the original polyimide coating. The top of figure 3 illustrates the size of a shrunken PTFE sleeve relative to a PI-coated fiber. The bottom of figure 3 shows a close-up of a PTFE-wrapped fiber sensor adjacent to a typical polyimide-coated fiber. A typical K-type thermocouple (TC) is also shown in the bottom of figure 3, for size comparison.

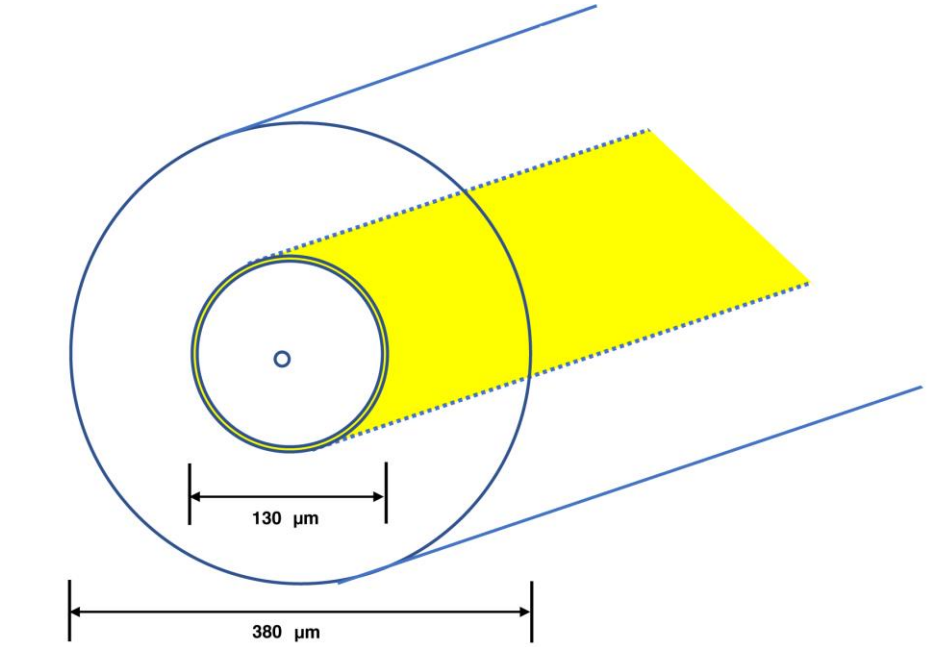

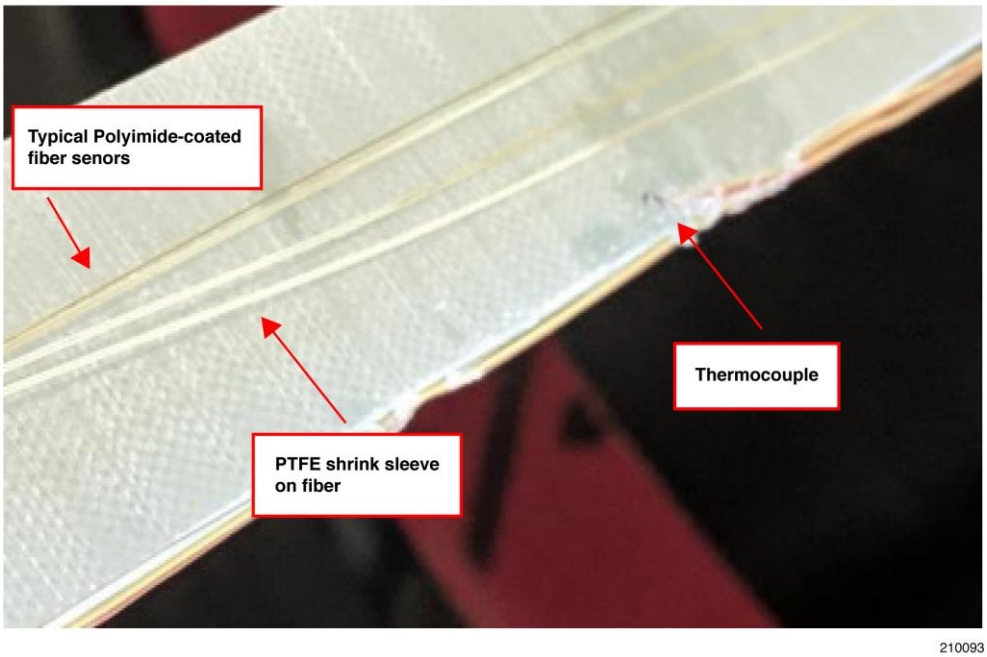

Figure 3. Illustration of the PTFE shrink sleeve over a typical polyimide-coated fiber sensor (top); and a close-up photograph of the PTFE shrink sleeve with typical polyimide-coated fiber sensors, and a typical K-type thermocouple (bottom).

Results and Discussion

Initial testing of the prototype sensor involving submerging the sensor in liquid nitrogen, with a constant liquid temperature of 78 K under atmospheric pressure, was conducted at AFRC. Figure 4 shows the setup of the experiment. Both the prototype PTFE-wrapped fiber (hereafter, “PTFE-fiber”) and a typical polyimide-coated fiber array (hereafter, “PI-fiber”) were guided on a custom fiberglass rake instrumented with six K-type thermocouples. These thermocouples served as a known-source temperature measurement. Each sensor was separated by five inches from the other, except for the first sensor, which was one inch from the tip of the rake. The fibers were ensured to remain straight within the rake by way of a custom ring-guide, which also served to ensure that no external strain was applied to the fiber due to contraction. The rake was slowly inserted into the Dewar to ensure minimal liquid boil-off. Afterward, the liquid nitrogen was slowly evaporated within the Dewar, such that the temperature change from within the Dewar could be recorded.

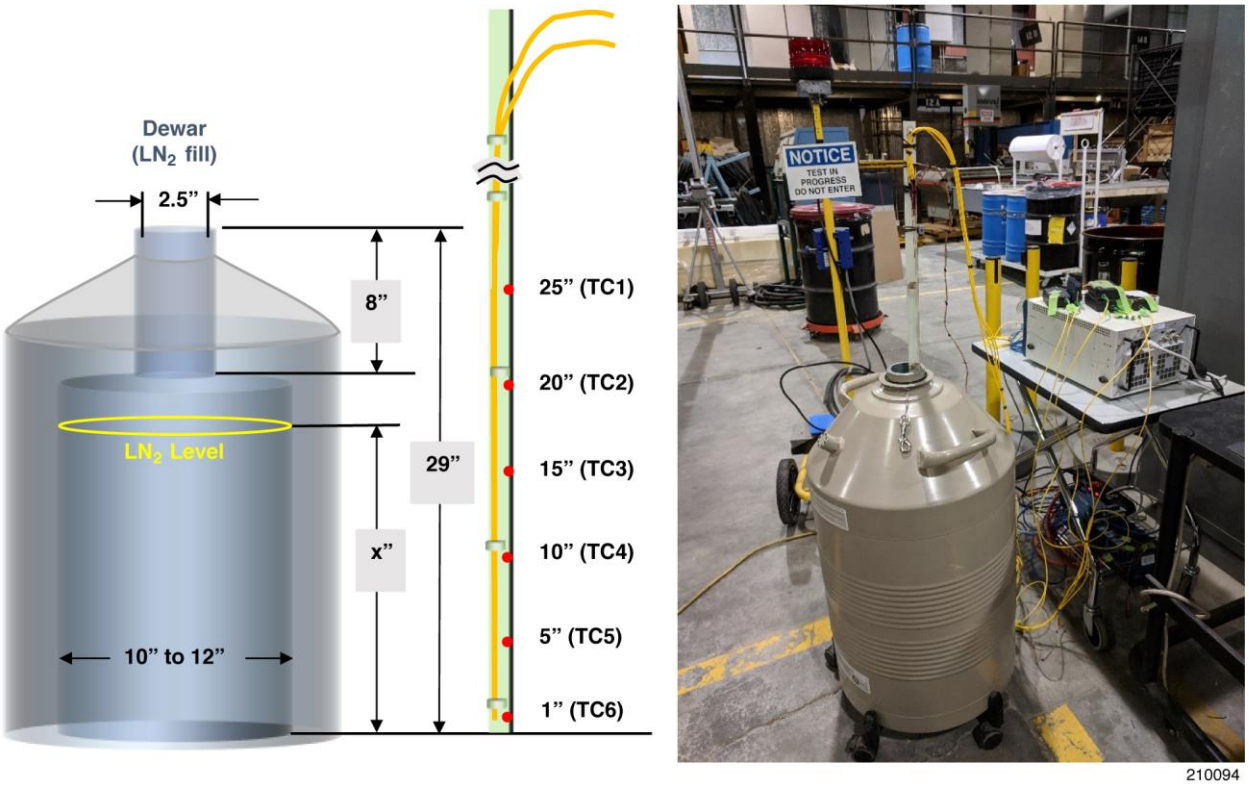

Figure 4. The setup of the liquid nitrogen Dewar for the time-lapse experiment.

Figure 5 shows the time-lapse wavelength-shift measurement of the PI-fiber as well as for the PTFE-fiber. The PI-fiber experienced -1.6 nm of wavelength shift while the PTFE-fiber experienced - 5.2 nm of wavelength shift from ambient temperature to liquid nitrogen. A consistent four-grating (approximately two inches) shift of data across both sets of data can be seen; most of the grating shifts occurred in the first hour of the time lapse. Thus, the insertion of the cryo-rake into the Dewar caused substantial evaporation within the first hour of the experiment; after the first hour the temperature distribution inside the Dewar gradually stabilized over the next two hours.

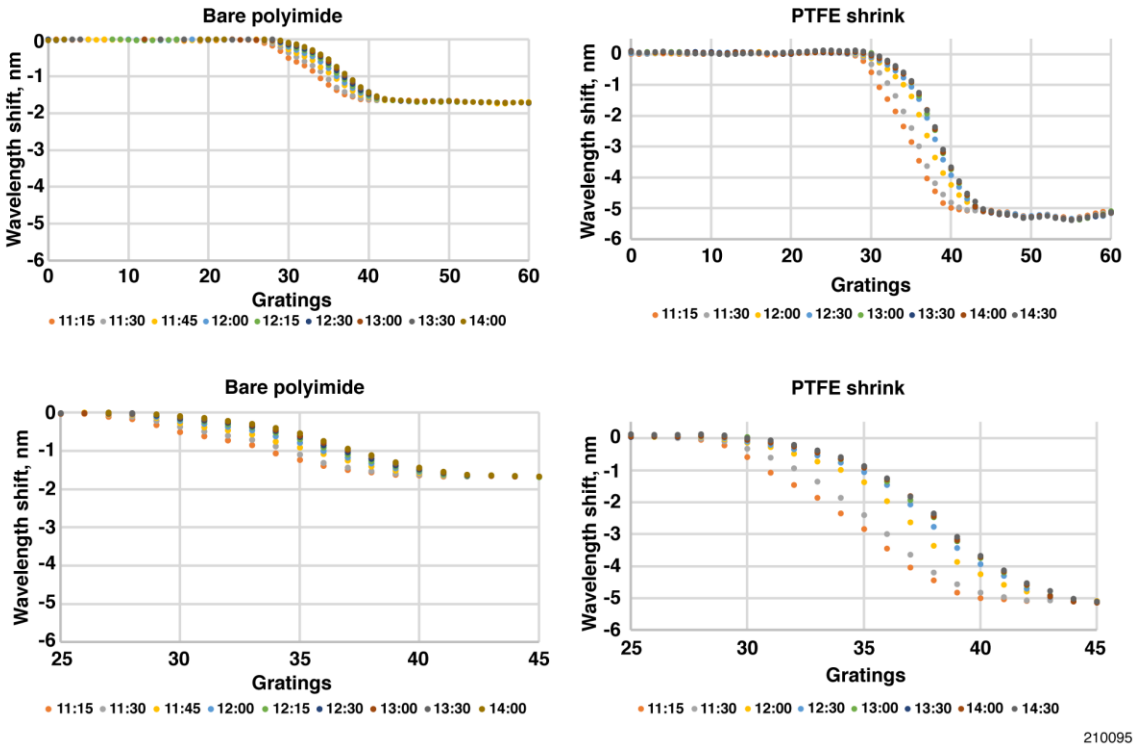

Figure 5. The time-lapse wavelength shift of (top left; close view bottom left) the polyimide-coated fiber grating arrays; and, (top right; close view bottom right) the PTFE-shrink fiber grating array submerged in the Dewar of liquid nitrogen. Over three hours of continuous acquisition, there were two inches (four gratings) of evaporation of the liquid nitrogen measured by way of the wavelength shift.

The relationship of temperature versus wavelength shift between PI-fiber and PTFE-fiber can be plotted by obtaining the K-type TC data that correlate to the adjacent fiber sensor (fig. 6). The temperature data range that can be obtained is limited by the TC that resides in the ullage region on the top portion of the Dewar, as the temperature of TC submerged under liquid nitrogen stays consistent. A linear-fit graph shows the slope of the fiber, where the PI-fiber has a wavelength response of 7.3pm/K. The PTFE-fiber has a wavelength response of 23.4pm/K - approximately three time more responsive than the PI-fiber sensor. In order to better characterize the fiber-to-temperature response over a consistently large cryogenic temperature range, the fiber is tested using a cryostatic vacuum to simulate a cryogenic environment.

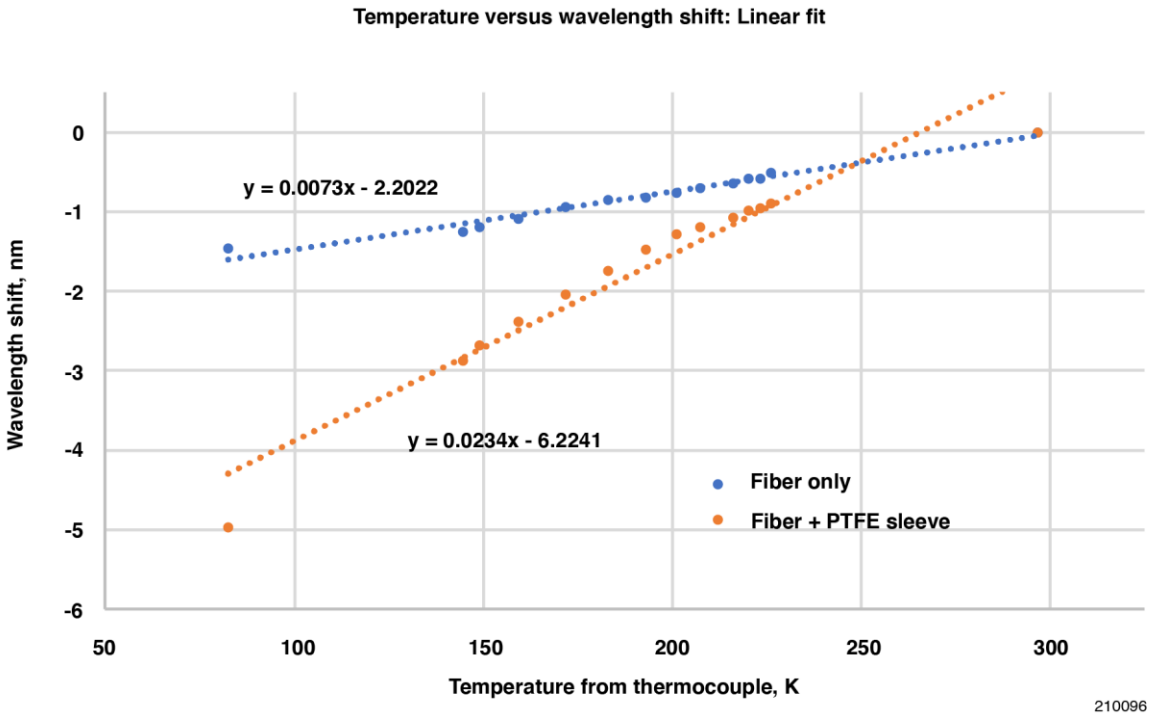

Figure 6. The linear fit of wavelength shift versus temperature from thermocouple between the polyimide-coated fiber (fiber only) and the shrink-sleeved-wrapped fiber (Fiber + PTFE sleeve) under liquid nitrogen evaporation.

Figure 7 shows the cryostatic testing setup, conducted at the NASA Ames Research Center (Moffett Field, California). A custom copper enclosure was mounted on top of a cold head, where it was cooled by a cryocooler running helium. A calibrated silicon diode from Lake Shore Cryotronics (Westerville, Ohio) was mounted on the copper enclosure to continuously monitor the temperature of the substrate. The PTFE-fiber and the PI-fiber were placed on top of the copper plate. A limited amount of Apiezon-N® (M&I Materials, Limited Manchester, United Kingdom) cryo-grease was used to bond the fiber to the copper enclosure, to provide surface contact but prevent unintentional apparent strain caused by the contraction of the grease.

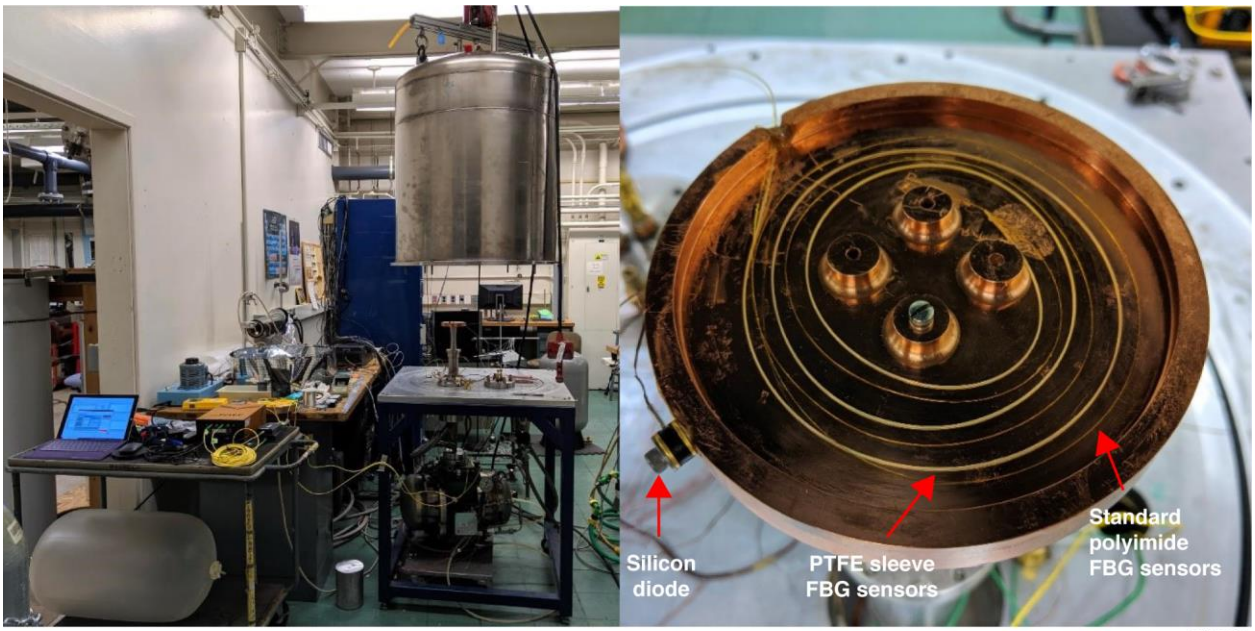

Figure 7. The cryostatic bell jar with the cold head (left); and a close-up view of the fiber sensors and the silicon diode placed on top of the copper enclosure mounted on the top of the cold head (right).

A description of simulated cryo-static measurement follows. The bell jar is lowered. A vacuum up to 10^{-6} Torr is achieved by way of, first, a rough pump and, next, an ion pump. The cryocooler is turned on, pumping liquid helium to the cold head inside the vacuum inside the bell jar. The copper enclosure along with the fiber is bolted to the cold head, and in the process is cooled from the ambient temperature (297 K) down to 15 K. After the low temperature is achieved and has stabilized for an hour, the cryopump is turned off and the sample is naturally warmed, slowly ramping up back to the ambient temperature. Figure 8 shows and compares the temperature change of the silicon diode versus the selected sensor of the two testing fibers in terms of center wavelength shift, wherein the PTFE-fiber has a higher wavelength change compared to the PI-fiber.

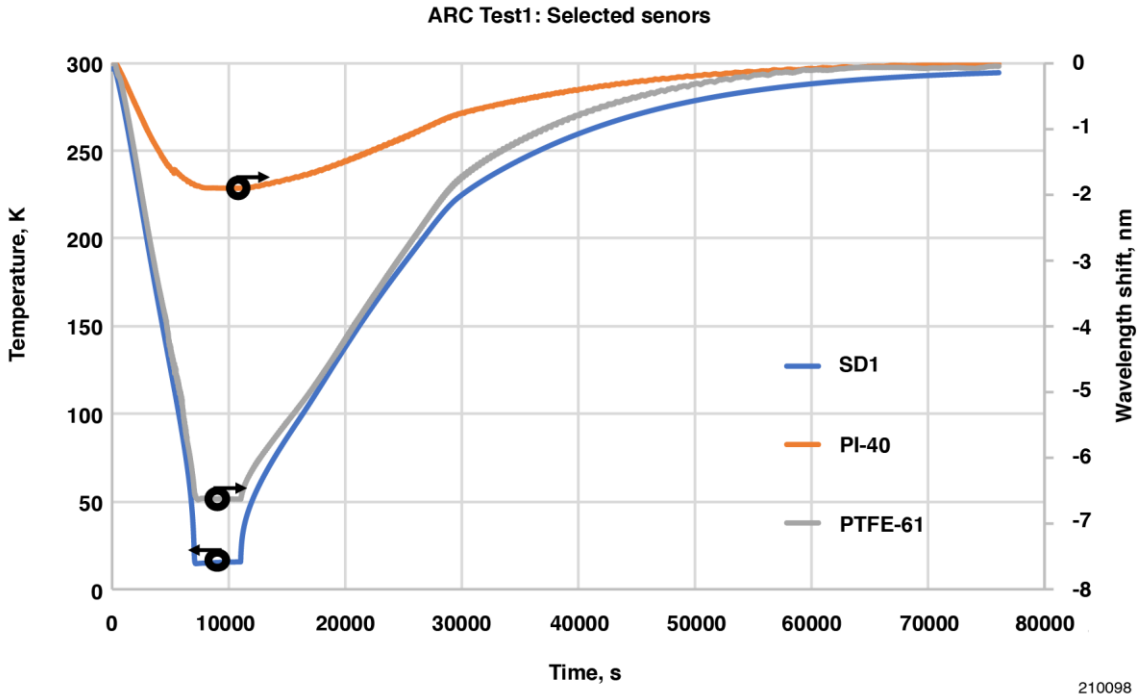

Figure 8. The testing profile for selected grating in terms of wavelength shift (right column y-axis) compared to silicon diode temperature (left column y-axis) under a specific time period.

Figure 9 and figure 10 demonstrate the cool-down as well as the warm-up profile across the fiber sensors. The unevenness of application of the cryo-grease to the fibers, and the tendency of the cryo-grease to create a large apparent strain when the grease hardened under cryogenic temperature, resulted in there being many fiber sensor locations at which the wavelength shift was not indicative of only the temperature shift. As shown by the cool-down profile of the PI-fiber, only when the temperature dropped below 50 K (the cryo-grease had completely frozen) could the fiber sense correctly the temperature of the copper enclosure. A specific sensor for each fiber (PI-fiber #40, and PTFE-fiber #61) was selected to characterize the wavelength change as its cool-down and warm-up, respectively.

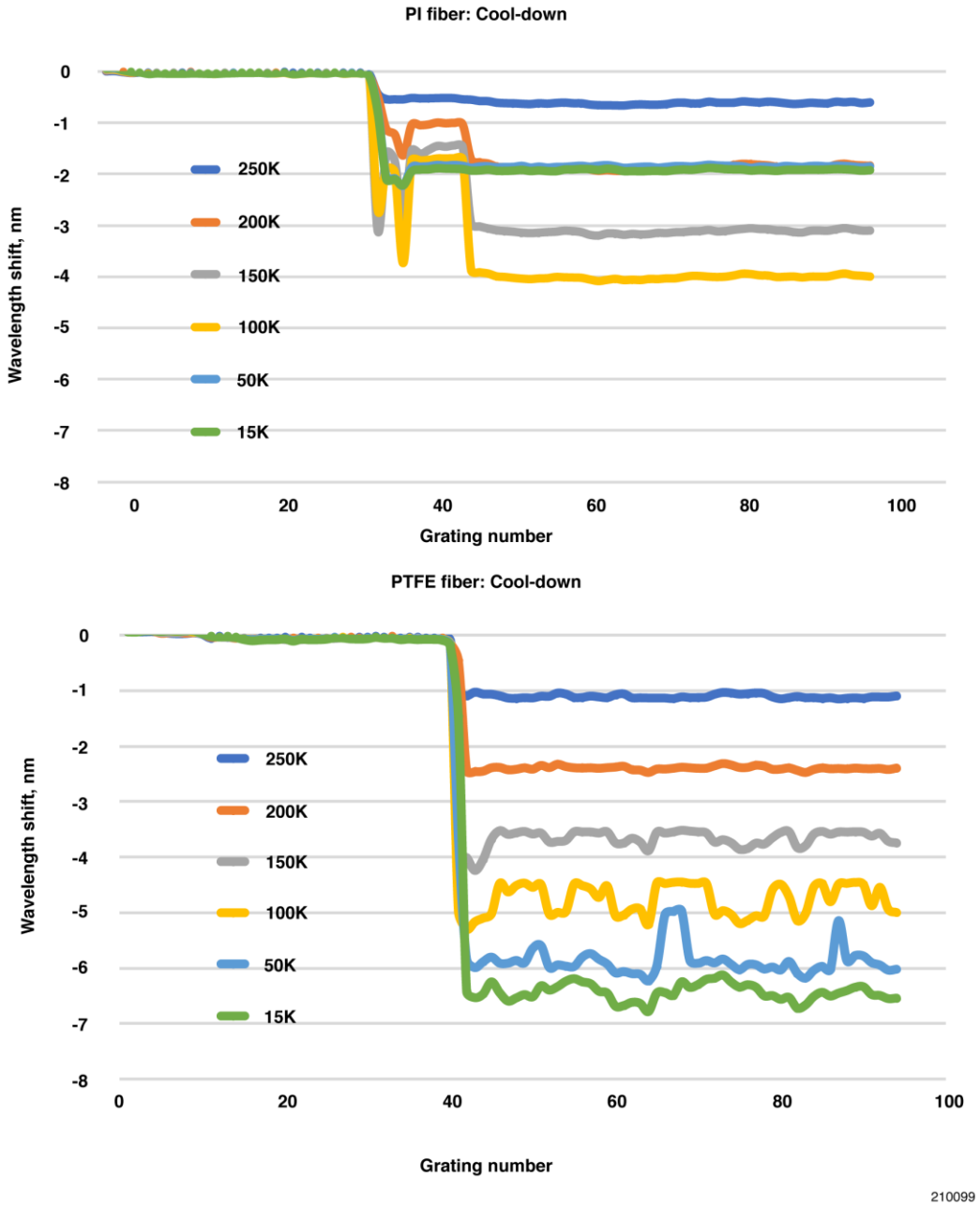

Figure 9. The cool-down profile for the PI-fiber (top) and the PTFE fiber (bottom) from 250 K to 15 K. The effect of additional apparent strain caused by the contraction of the cryo-grease contributed to the additional wavelength shift on the cool-down process in most of the PI-fiber sensors.

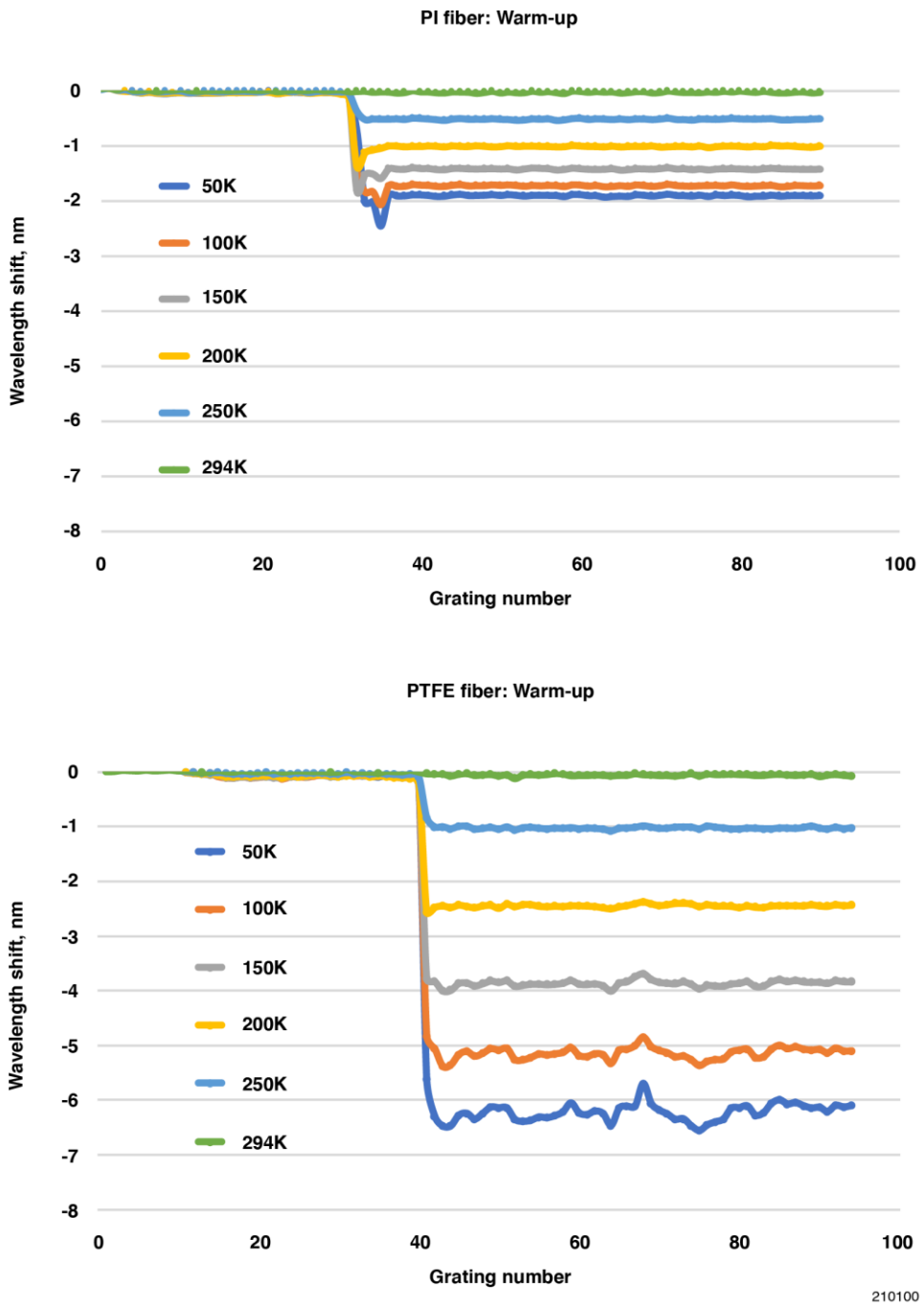

Figure 10. The warm-up profile for the PI fiber (top) and the PTFE fiber (bottom) from 50 K back to 294 K.

The wavelength shift values of the two fiber sensors are plotted with respect to the silicon diode temperature response in figure 11. A second-degree polynomial fit describes the wavelength shift for both sensors. The PI-fiber exhibits a reduction in temperature sensitivity below 100 K, whereas the PTFE-fiber has a relatively linear response from 297 K all the way down to 20 K.

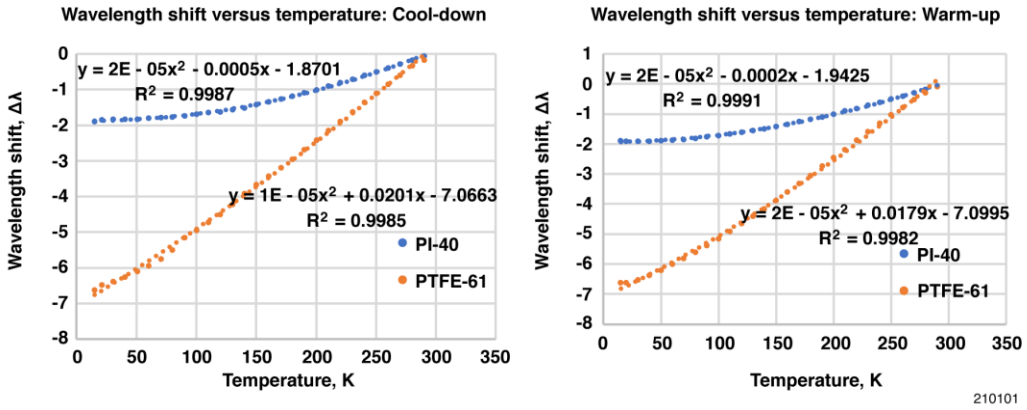

Figure 11. The cool-down (left) and warm-up (right) profile for the polyimide-coated fiber sensor (PI-40) and the PTFE-wrapped fiber sensor (PTFE-61).

In order to describe the reduction in sensitivity under reduced temperature, two linear fits are used in figure 12. The first case demonstrates the linear fit from 275 K to 100 K, and the second case from 100 K down to 15 K. The slope of the linear fit is the effect of the wavelength shift of the fiber with respect to temperature shift, where a larger slope means better temperature sensitivity. For the PI-fiber, the slope corresponds to 8.5pm/K. For the PTFE-fiber, the linear fit slope is 25.7pm/K, which agrees with the three-times improvement result given by the previous long-term liquid nitrogen Dewar evaporation testing. The reduced performance of the PI-fiber can be seen by observing the second-case linear fit from 100 K down to 15 K. The wavelength shift response for the PI-fiber drops from 8.5pm/K to 2pm/K, which equates to a 76-percent loss of sensitivity compared to elevated temperature. Similarly, the wavelength response of the PTFE-fiber drops from 25.7pm/K to 19.2pm/K in the second case - a 25-percent loss of sensitivity. Comparing both fiber sensor under 100K, the PTFE-fiber is approximately 10 times more sensitive than the PI- fiber, which indicates that fiber sensing is more viable at these cryogenic temperatures.

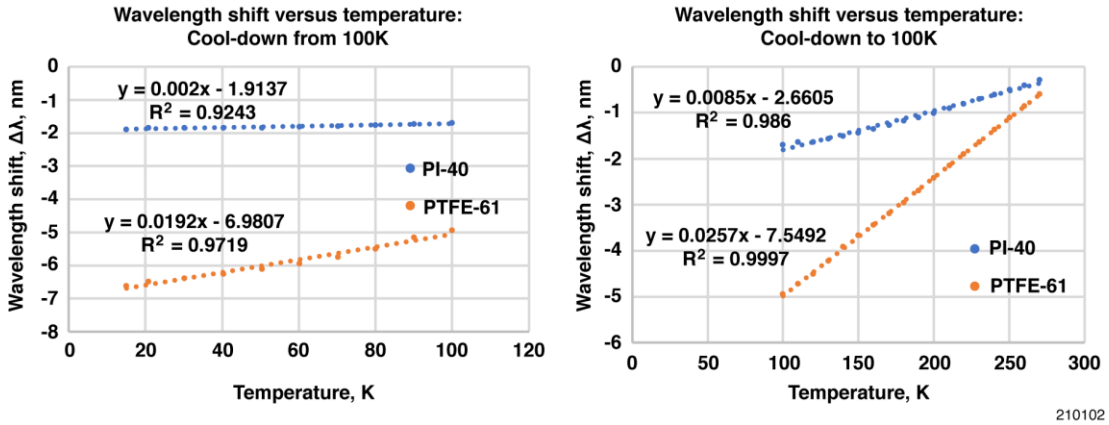

Figure 12. Linear fit of the cool-down wavelength shift profile from 15 K to 100 K (left); and from 100 K to 297 K (right). From ambient temperature (297 K) down to 100 K, the slope is 8.5pm/K for the standard polyimide-coated fiber (PI-40), and 25.7pm/K for the PTFE-wrapped fiber (PTFE-61). From 100 K to 15 K, the slope dropped to 2.0pm/K for the standard polyimide-coated fiber (PI-40), and to 19.2pm/K for the PTFE-wrapped fiber (PTFE-61).

A separate testing under a cryostat filled partly with liquid nitrogen and pressurized by inserting nitrogen gas from 15 psig to 45 psig was conducted at the NASA Marshall Space Flight Center (Huntsville, Alabama). The two fibers were hung from the top of the cryostat, as shown in figure 13. Eight Lake Shore silicon diodes were concurrently mounted on a separate metallic rake, each diode three inches from the other. Table 1 lists the corresponding fiber sensor location with respect to the silicon diode.

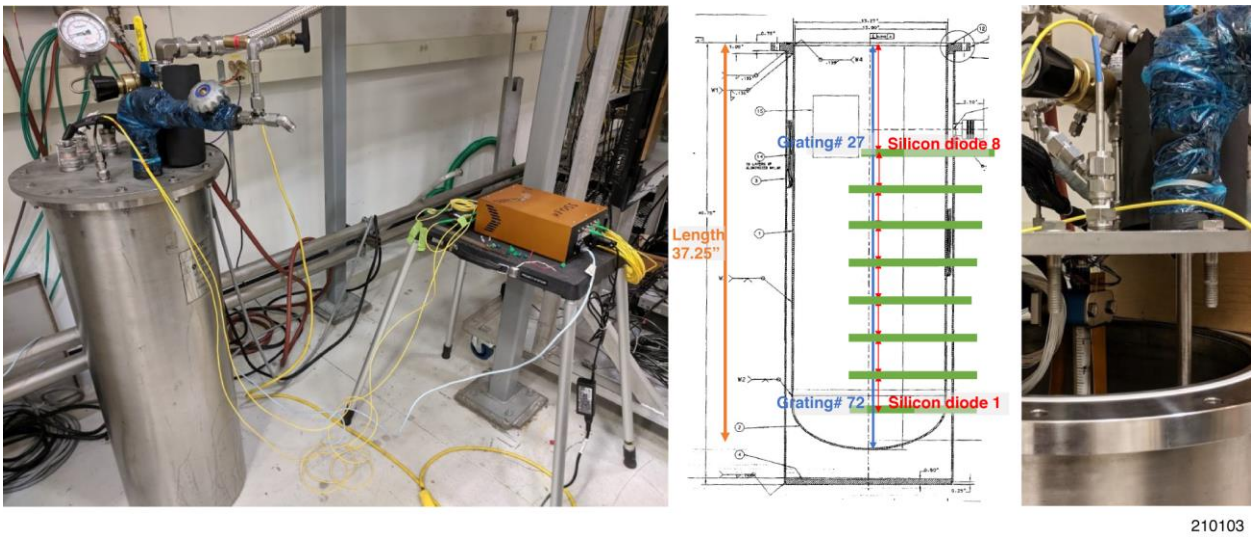

Figure 13. Left, cryostat pressurization testing under liquid nitrogen; center, the schematics of the location of the silicon diode rake versus the corresponding fiber sensor grating array location from the top of the lid downward; and, right, a close-up view of the fiber sensor and the silicon diode rake.

Table 1. The location of the silicon diode with respect to the corresponding fiber gratings being tested.

Diode number	Distance from top, in	Grating number, rounded
8	13.0	27
7	16.5	34
6	19.0	40
5	22.5	47
4	25.5	53
3	28.5	60
2	31.5	66
1	34.3	72

Figure 14 shows the cryostat internal pressure with respect to time. The internal pressure of the cryostat was increased by adding ambient temperature nitrogen gas; however, adding this warm gas caused liquid nitrogen to boil off, which increased internal pressure of the tank. Excess gas was manually vented to ensure the internal pressure was stabilized. Periods of pressure instability were seen after more nitrogen gas was added onto the tank. As the pressure varied, both fiber sensors and the silicon diode were able to record the temperature fluctuation;

however, the fiber sensors took a more pronounced initial temperature response compared to the silicon diode, due to the lack of a metallic thermal sink associated with the silicon diode rake. As expected, the PTFE-fiber had a higher wavelength-shift response than did the PI-fiber, due to both a higher CTE value of the PTFE, and the addition of thicker PTFE-wrap, compared to the thin polyimide-only coating.

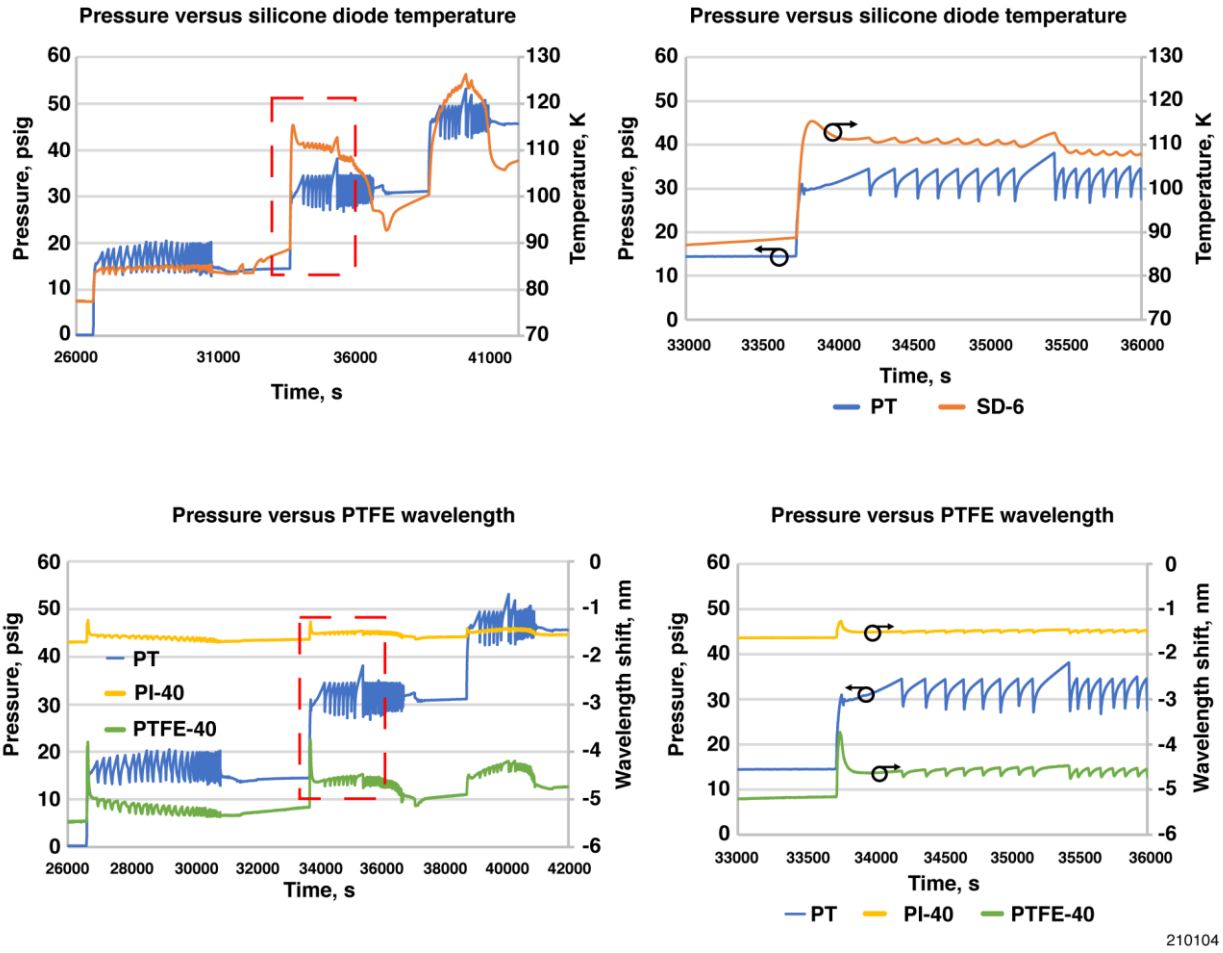

Figure 14. Top left, the cryostat internal pressure (PT) changes (left y-axis) with respect to the temperature changes (right y-axis) of the silicon diode (SD-6). Top right, a close-up of the thermal response (corresponding to the area enclosed by the dashed red lines) of the silicon diode (arrow pointing at right y-axis) as a result of unstable internal pressure (left y-axis). Bottom left, the cryostat internal pressure (PT) versus the PI-fiber (PI-40) and PTFE-fiber (PTFE-40) sensors at the identical time period. Bottom right, a close-up of the fiber sensor response (corresponding to the area enclosed by the dashed red lines) under unstable internal pressure.

From the data obtained through the cold-head cryostat testing, a third-degree polynomial fit for both fibers was obtained by inverting the wavelength shift data versus temperature (fig. 15). These empirical equations became a calibration curve with which to compare wavelength shift to temperature changes. By comparing the wavelength shift at a steady pressure point at the pressurized cryostat chamber (15, 30, and 45 psig, respectively), the temperature profile for the fiber sensors was curve-fitted by way of a third-order polynomial. The curve-fit equations were then compared with the silicon-diode rake measurement, shown in figure 16. Consistently, the temperature response of the PTFE-fiber sensors matched well with respect to the silicon-diode

rake, as opposed to the standard polyimide, except where a dislocation occurred at approximately the 28-in mark on the PTFE prototype that adversely affected the result further down-hole through the cryostat. As opposed to a coarse temperature profile using eight silicon diodes, a detailed temperature profile of the cryostat at approximately .05-in intervals could be accurately captured via the PTFE-wrapped fiber sensors.

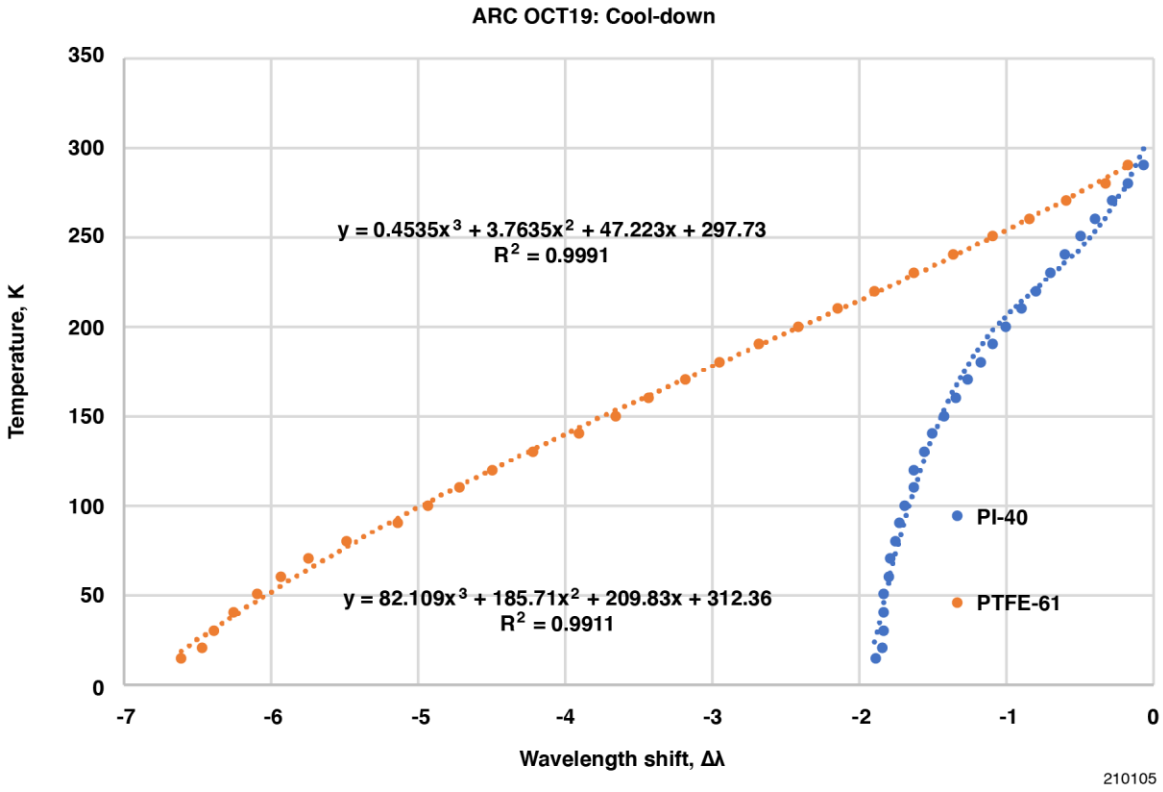

Figure 15. The empirical third-order polynomial equation used to coordinate the wavelength shift to a corresponding temperature for both types of fiber sensors from prior cryostatic calibration testing.

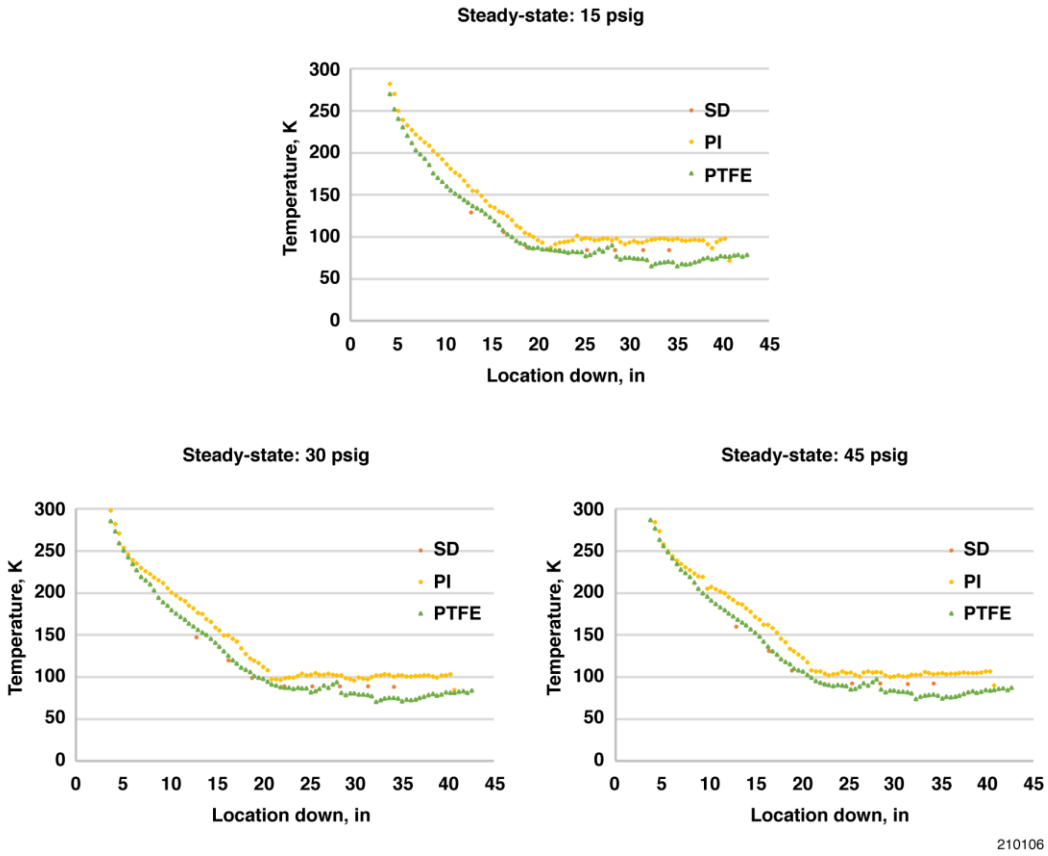

Figure 16. The steady-state temperature distribution downward (from the top of the cryostat), measured by eight silicon diodes (SD), and derived using the wavelength shift from the polyimide-coated fiber (PI) and the PTFE-wrapped fiber (PTFE).

Figure 17 compares the temperature measurement of the silicon diode rake versus the corresponding PTFE-fiber sensor as the cryostat was filled with liquid nitrogen and pressurized with nitrogen gas. Silicone diodes 8 through 6 measured the ullage temperature, while silicone diode 5 measured the liquid nitrogen temperature. As ambient nitrogen gas was pumped to the cryostat, the ullage temperature rose. The dynamic temperature response of the fiber sensors was faster than that of the silicon diodes, because the silicon diodes mounted to the metal rake act as a heat sink. The temperature fluctuation of the fiber sensors at the ullage portion (PTFE-27, PTFE-34, and PTFE-40) was much more varied compared to the corresponding silicon diode during hot gas insertion.

For the PTFE-fiber sensor, tracking with silicone diode 5 was within +/- 1K throughout most of the testing, where the temperature range was predominantly below 100 K. Worst-case tracking occurred on silicone diode 8, where the fiber sensor temperature was 10 K higher than that of the corresponding silicon diode. Discrepancies of fiber temperature measurement versus silicon diode are still under investigation. One of the causes might be a lack of uniformity among the PTFE-fiber sensors; a unique temperature calibration curve might be need for each sensor throughout the PTFE-fiber array.

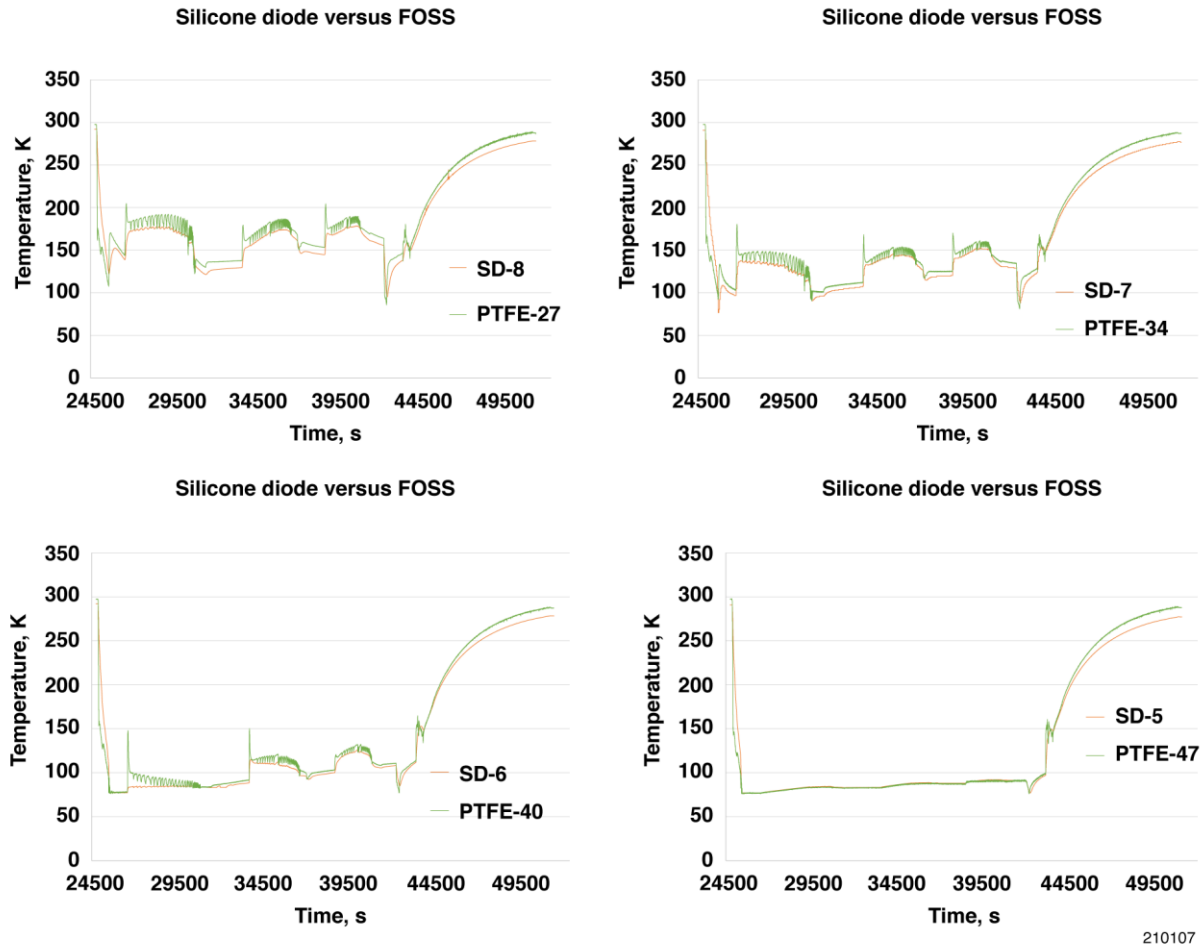

Figure 17. Comparison of the temperature response of specific silicon diodes (SD-8, SD-7, SD-6, SD-5) with the corresponding fiber sensor counterpart (PTFE-27, PTFE-34, PTFE-40, PTFE-47) within the same time period. The dynamic temperature response of the fiber sensor is consistently faster than that of the silicon diode, as shown by the absence of the temperature fluctuation from the time.

Conclusion

The challenge of fiber optic temperature response under cryogenic condition is well-known; fiber Bragg grating sensors coated with a thin polyimide coating suffer up to a 75-percent loss of thermal response at temperature under 100 K: from 8.5pm/K at 297 K to 2.0pm/K at 80 K. The temperature sensitivity of the fiber sensor can be improved by increasing the coating diameter as well as selecting a material with a higher coefficient of thermal expansion. This report describes a novel, simple-to- fabricate polytetrafluoroethylene (PTFE)-based fiber sleeve, the thermal sensitivity of which is three times higher than polyimide-coated fiber to 25.7pm/K at 297 K. At temperatures lower than 100 K, the thermal sensitivity decreases only by 25 percent; as well, the PTE-based fiber is ten times more sensitive than the polyimide-coated fiber. Calibration using industry silicon diodes was conducted in a pseudo-cryostatic environment, and side-by-side fiber sensor performance with silicon diodes under liquid nitrogen was considered. Future research plans include improvement in sensor-to-sensor temperature accuracy with respect to silicon diodes, which might be achieved by a pre-sensor wavelength-shift-to-temperature calibration effort.

References

1. Grattan, K. T. V., and B. T. Meggitt, eds., *Optical Fiber Sensor Technology Fundamentals*, Kluwer Academic Publishers, 18-19, (2000).

2. Richards, W. Lance, Allen R. Parker, Jr., William L. Ko, Anthony Piazza, and Patrick Chan, “Application of Fiber Optic Instrumentation,” NATO RTO-AG-160-V22, July 2012.

3. Parker, Allen R., Jr., “Method for Reducing the Refresh Rate of Fiber Bragg Grating Sensors.” Patent no. US 8,700,358, April 15, 2014.

4. Hamory, et al., “Wavelet-based Processing for Fiber Optic Sensing Systems,” Patent No. US 9,444,548, September 13, 2016.

5. M. Froggatt and J. Moore, “Distributed measurement of static strain in an optical fiber with multiple Bragg gratings at nominally equal wavelengths,” *Applied Optics,* Vol. 37, No. 10, 1998, pp. 1741-1746.

6. James, S. W., M. L. Dockney, and R. P. Tatam, “Simultaneous independent temperature and strain measurement using in-fibre Bragg grating sensors,” *Electronics Letters,* Vol. 32, No. 12, 1996, pp. 1133-1134.

7. Wu, Meng-Chou, and William H. Prosser, “Simultaneous Temperature and Strain Sensing for Cryogenic Applications Using Dual-Wavelength Fiber Bragg Gratings,” *Proceedings of SPIE,* Vol. 5191, 2003, pp. 208-213.

8. Habisreuther, Tobias, et al., “ORMOCER Coated Fiber-Optic Bragg Grating Sensors at Cryogenic Temperatures," *IEEE Sensors Journal,* Vol. 12, No. 1, 2012, pp. 13-16.

9. Weisbrich, Martin, and Klaus Holschemacher, “Comparison between different fiber coatings and adhesives on steel surfaces for distributed optical strain measurements based on Rayleigh backscattering,” *J. Sens. Sens. Syst.,* 7, 2018, pp. 601-608.

10. Wu, Meng-Chou, Ruth H. Pater, and Stanton L. DeHaven, “Effects of coating and diametric load on fiber Bragg gratings as cryogenic temperature sensors,” *Proc. of SPIE,* Vol. 6933, 2008, pp 693303-1 - 693303-10.

11. Lupi, C., et al., “Metal coating for enhancing the sensitivity of fibre Bragg grating sensors at cryogenic temperatures,” Technical Note, *Smart Mater. Struct.,* Vol 14, 2005, pp. N71-N76.

12. Wu, Meng-Chou, and Stanton DeHaven, “High-sensitivity cryogenic temperature sensors using pressurized fiber Bragg gratings,” *Proc. of SPIE,* Vol. 6189, 2006, pp. 61890O-1 - 61890O-7.